Numerical Investigations of a Transitional Flat-Plate Boundary Layer with Impinging Shock Waves

Alessandro Pagella, Ulrich Rist, Siegfried Wagner
Institut für Aerodynamik und Gasdynamik
Universität Stuttgart
Germany

Abstract

The transitional behaviour of a flat-plate boundary layer with shock-boundary layer interaction has been investigated for both small-amplitude and weakly non-linear disturbances at $Ma = 4.8$ with constant wall temperature and $Ma = 4.5$ with insulated wall, respectively. The separation bubble induced by the impinging shock wave remained steady in both situations. In the linear case, compressible linear stability theory results have been calculated and compared with direct numerical simulations. The two results agree well, if non-parallel effects already present in the same boundary layer without impinging shock wave are considered. Maximum amplification rates were increased and shifted to lower disturbance frequencies. In the weakly non-linear case, fundamental, subharmonic and oblique scenarios were simulated. It was found, that in all three cases the $(0, k)$-modes, the so-called vortex- or streak modes were strongly amplified downstream of reattachment. This might be triggered by a Görtler-type instability, which could be caused by the concave curcature of the boundary layer at reattachment. However, this statement remains to be proved.

List of Symbols

"∞"	indicates dimensional free-stream values
A/A_0	amplitude ratio of any flow variable
c_f	skin friction coefficient
c_p, c_v	specific heats at constant pressure, volume
e	energy
f^*	dimensional disturbance frequency
F	disturbance frequency $= (2\pi f^* L)/(u_\infty Re)$
F_0	fundamental disturbance frequency
h	frequency mode in Fourier space
k	spanwise Fourier mode
L	dimensional reference length
Ma	Mach number
p	pressure
Pr	Prandtl number
Re	global Reynolds number $= (\rho_\infty u_\infty L)/\mu_\infty$
R_x	local Reynolds number $= \sqrt{xRe}$
t	time
T	temperature
T_s	Sutherland temperature
T_w	wall temperature
u	streamwise velocity component
v	wall-normal velocity component
w	spanwise velocity component
x	streamwise coordinate
y	wall-normal coordinate
z	spanwise coordinate
$-\alpha_i$	streamwise amplification rate
α_r	streamwise wave number
β	spanwise wave number
ϑ	thermal conductivity coefficient
κ	specific heat ratio
μ	viscosity
ρ	density
σ	shock angle with respect to x

ω_x	x-component of the vorticity
ψ	obliqueness angle of the disturbances

Introduction

In trans-, super- and hypersonic flight conditions, shock-boundary layer interactions are omnipresent. Research on the properties of such flows began as early as mankind started to develop the knowledge and technology for flying beyond the sound barrier in the late 1930's and early 1940's. In 1946, Ackeret, Feldmann and Rott (Ref 1) and Liepmann (Ref 15) performed the first systematic experimental studies, and a lot of work has been done in the late 1940's and 1950's by scientists in countries of both the then East and West.

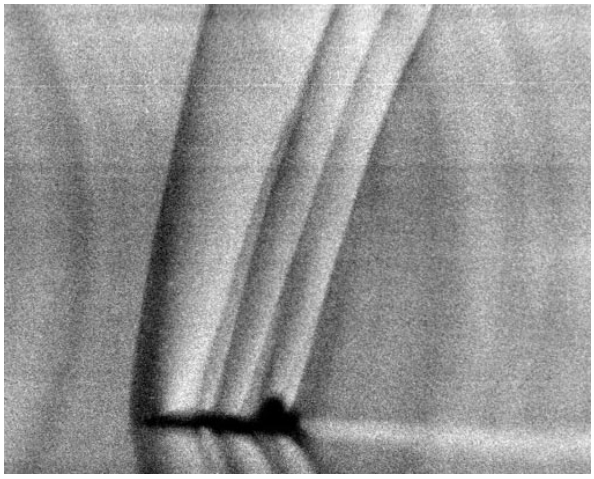

Figure 1: Schlieren photograph of T-38 shock waves at $Ma = 1.1$, 13000 feet. Photo is courtesy of NASA Dryden Research Center Photo Collection. NASA Photo: EC94-42528-1, December 13, 1993. Photo by: Dr. Leonard Weinstein

Figure 1 shows a Schlieren photograph of a T-38 experimental aircraft at low supersonic speed. The image gives an idea of the importance of shock-phenomena in such flows. For example, shock-boundary layer interaction plays an important role in terms of the performance of jet-intakes, which have to decelerate the incoming flow from super- to subsonic speed. On the wings of modern passenger aircraft flying at high subsonic speed, local supersonic flow regions occur under certain flight conditions. These are terminated by an almost vertical shock, which influences the local flow properties. In internal flows like turbomachinery, shock-boundary layer interactions are present as well, as it can be seen in Fig 2.

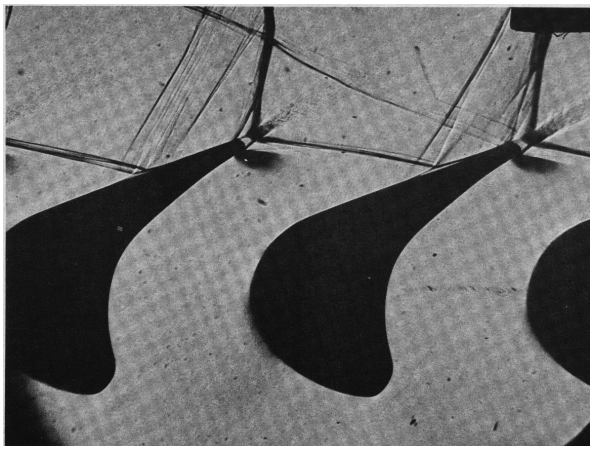

Figure 2: Photograph of a turbine rotor (Ref 9).

After the second half of the 1950's and in the 1960's, technical progress seemed to have no limits. Because of the ability to perform space flights, the possible speed for technical applications extended to the hypersonic range, which made the prediction of thermal and pressure loads an issue, to which the structure is exposed during re-entry. In Fig 3, the four shadowgraphs represent early re-entry vehicle concepts. It was found, that a blunt body produces a shock wave in front of the vehicle that shields the vehicle from excessive heating, reducing the thermal load compared to a pointed design. Because of the higher temperatures in hypersonic flight conditions, real-gas effects become important, too.

The authors would like to refer to more thorough discussions of the properties of flows with shock-boundary layer interaction, which can be found e.g. in (Ref 4), (Ref 5) and (Ref 6). Although a lot of problems have been solved during the last decades of research in this particular field, a number of questions still remain unanswered while seemingly clarified problems led to new issues. In his review about achievements and unresolved problems of shock-boundary layer interactions, Dolling (Ref 6) named one of those yet unresolved issues as the transitional behaviour of

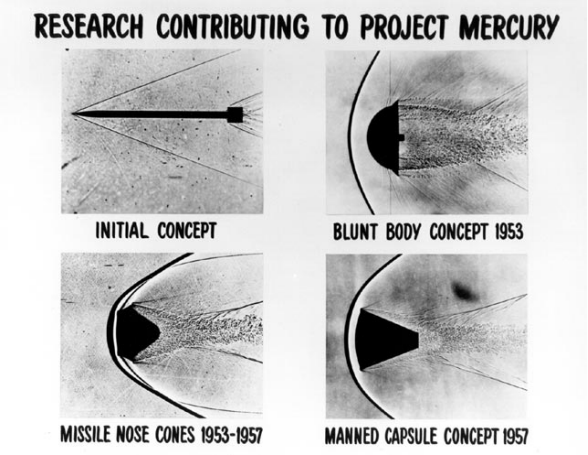

Figure 3: Photographs of early re-entry design concepts. Picture is courtesy of NASA, GRIN DataBase Nr. GPN-2000-001938.

such flows. The work, done for this paper intends to contribute some investigations to this particular field.

The transition process for compressible flows can be classified into several merging stages, similar to incompressible flows. The first phase of transitional development in a low free-stream disturbances environment, the amplification of disturbances with small amplitudes was pioneered by Lees and Lin (Ref 13) in 1946 and later extended by Mack (Ref 16). The next phase of the transition process, which follows the linear regime, can be explained in a similar but more complicated manner compared to incompressible flows. In incompressible boundary layers, after the two-dimensional Tollmien-Schlichting waves, which are exponentially amplified have reached sufficiently large amplitudes, a non-linear, three-dimensional development takes place. Small-amplitude three-dimensional disturbances become amplified and a periodic structure appears in spanwise direction. This stage is called secondary instability, which can be quantitatively described by Floquet theory (Ref 12). Eventually, so-called lambda vortices form in a later development. Locally, high shear stresses occur, which are later breaking into several small structures, resulting in turbulent spots. These move downstream, grow and finally develop into the fully turbulent flow. A good insight into hypersonic transition is given by Saric, Reshotko and Arnal (Ref 17). However, transition under super- and hypersonic conditions is far from beeing understood and results of transional flows with shock-boundary layer interactions are not known to the authors.

Numerical Scheme

Governing equations The numerical scheme is based on the complete, three-dimensional, unsteady, compressible Navier-Stokes equations for cartesian cordinates in conservative formulation:

$$\frac{\partial \rho}{\partial t} + \nabla \cdot (\rho \mathbf{u}) = 0 \quad (1)$$

$$\frac{\partial (\rho \mathbf{u})}{\partial t} + \nabla \cdot (\rho \mathbf{u}\mathbf{u}) + \nabla p = \frac{1}{Re} \nabla \cdot \sigma \quad (2)$$

$$\frac{\partial (\rho e)}{\partial t} + \nabla \cdot (p + \rho e)\mathbf{u} = \frac{1}{(\kappa - 1) Re Pr Ma^2} \nabla \cdot (\vartheta \nabla T) + \frac{1}{Re} \nabla \cdot (\sigma \mathbf{u}) \,, \quad (3)$$

where

$$\sigma = \mu \left[(\nabla \mathbf{u} + \nabla \mathbf{u}^T) - \frac{2}{3} (\nabla \cdot \mathbf{u}) \mathbf{I} \right] \quad (4)$$

with the velocity vector $\mathbf{u} = [u, v, w]^T$.

The energy is calculated as

$$e = \int c_v \, dT + \frac{1}{2}(u^2 + v^2 + w^2). \quad (5)$$

The fluid is a non-reacting, ideal gas with constant Prandtl number $Pr = 0.71$ and specific heat ratio $\kappa = c_p / c_v = 1.4$, with c_p and c_v as the specific heat coefficients at constant pressure and volume, respectively. Viscosity μ for temperatures above the Sutherland temperature T_s is calculated by Sutherland's law, for temperatures below T_s with the relation $\mu / \mu_\infty = T / T_\infty$. The thermal conductivity coefficient ϑ is proportional to the viscosity. In our simulations, all lengths are made nondimensional with a reference length L, which appears in the

global Reynolds number $Re = \rho_\infty * u_\infty * L/\mu_\infty = 10^5$. A local Reynolds number, which is used for the presentation of the results, is defined as $R_x = \sqrt{x * Re}$. The specific heat c_v is normalised with u_∞^2/T_∞ (with T_∞ giving the free-stream temperature) and time t is normalised with L/u_∞, where u_∞ is the free-stream velocity. Density ρ, temperature T and viscosity μ are standarized by their respective free-stream values.

Discretisation Time integration is performed at equidistant time steps with a standard Runge-Kutta scheme of fourth-order accuracy. In streamwise direction, compact finite differences of fourth-order accuracy are applied, which are in a split-type formulation in order to have some damping properties with regard to small-scale numerical oscillations, which occur at the high gradients resulting from the shock. In the split-type formulation, the weighting of the numerical stencil alternates each Runge-Kutta step from downwind to upwind and vice versa. If a stronger shock is applied, the damping characteristic of the split-type formulation is not sufficient enough. In this case, an implicit filter of fourth-order accuracy (Ref 14) is applied to filter the variables of the solution vector each physical time step in streamwise direction. In wall-normal direction split-type finite differences of fourth-order accuracy are used to calculate convective terms, while viscous terms are calculated by fourth-order central differences. In spanwise direction we have periodic boundaries, which allow to apply a spectral approximation with Fourier expansion. A more complete description of the discretisation can be found in (Ref 7).

Boundary and Initial Conditions At the free-stream boundary, a characteristic boundary condition (Ref 10) and, more recently, a non-reflecting boundary condition (Ref 18) is applied. The shock wave is introduced by holding the flow-variables constant in a limited area at the free-stream boundary, according to the Rankine-Hugoniot relations after the shock and the initial free-stream conditions before the shock. The inflow quantities at the inflow boundary result from the solutions of the compressible boundary layer equations and are held constant during the simulation. At the wall, a no-slip condition and vanishing normal velocities are assumed. Disturbances are introduced at the disturbance strip with simulated blowing and suction, given by the following equation:

$$f_{\rho v}(\xi, z, t) = \hat{a} * \sin(Ft) * \cos(k\beta z) * \sin(n\xi) * e^{-b\xi^2}, \quad (6)$$

with $-2\pi \leq \xi \leq 2\pi$ and $\xi = \pm 2\pi$ at the beginning and the end of the disturbance strip, respectively. In our modal discretization in spanwise direction, k indicates the spanwise Fourier modes, with $k = 0$ meaning a two-dimensional disturbance. The disturbance frequency F determines the streamwise wave number α_r via the dispersion relation of the disturbances. The spanwise wavenumber is β. Thus, the obliqueness angle ψ is given by $tan\,\psi = (k\beta)/\alpha_r$. The wall temperature can be chosen to remain constant or adiabatic.

Results

Unperturbed Base Flow In this paper, two cases of unperturbed, two-dimensional base-flows with shock-boundary layer interaction are considered. The first case is a $Ma = 4.8$ boundary layer with a free-stream temperature of $T_\infty = 55.4K$ and an impinging shock wave with a shock angle of $\sigma = 14^o$ relative to the x-axis. The wall temperature is held constant at $T_w = 270K$, which is equal to the adiabatic wall temperature of the same flow without shock. For this case, linear stability theory results and direct numerical simulations with small perturbation amplitudes will be shown in the next section.

Figure 4 displays the density gradient field and selected streamlines near shock-impingement. The shock causes the boundary layer to thicken. If a certain shock strength is exceeded, the boundary layer is not able to react to the pressure gradient of the shock without separating. This is the case in our two base-flow configurations. The impinging shock wave enters into the boundary layer. Until it ends at the sonic line as an almost vertical shock, its shock-angle becomes increasingly steeper because of the deceleration inside the boundary layer from the supersonic free stream

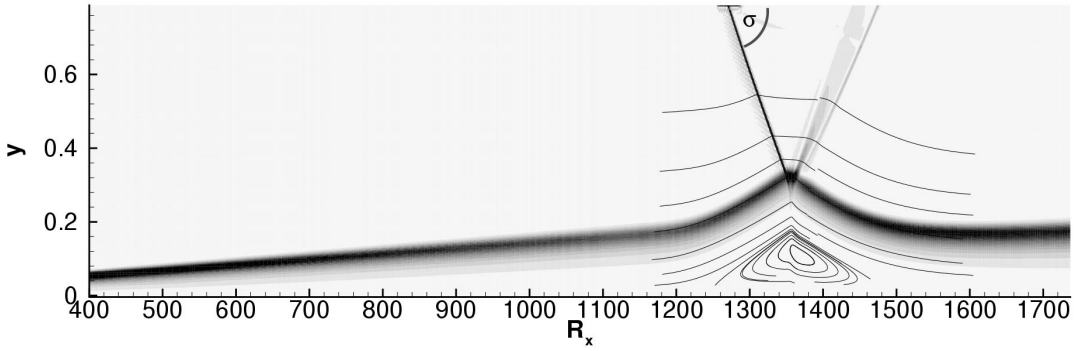

Figure 4: Density gradients $|\frac{\partial \rho}{\partial y}|$ and selected streamlines for $Ma = 4.8$, free stream temperature $T_\infty = 55.4K$ and constant wall temperature $T_w = 270K$ with a shock angle of $\sigma = 14^o$.

velocity to the sonic line. At the sonic line, it is reflected as a system of expansion waves.

Separation can be identified by taking a look at the skin friction, which is given in Fig 5 for the case of Fig 4. The negative skin-friction, which ranges from $R_x \approx 1240$ to $R_x \approx 1470$ indicates the separation bubble. The separation bubble in the baseflow remains steady for all cases investigated here. Its shape can be judged from the corresponding streamlines in Fig 4. Near separation and reattachment additional compression waves coalesce to the separation and reattachment shock well outside the boundary layer, respectively. However, these compression waves are relatively weak here and therefore can not be detected in Fig 4 but it can be seen in Fig 16, which shows an unsteady case with a stronger shock therefore beyond the scope of the present paper but briefly discussed in the section, were planned future work is described.

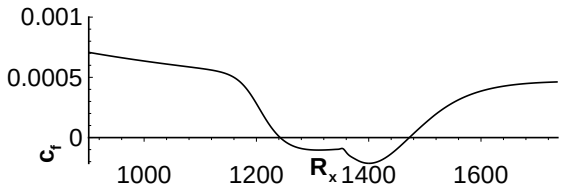

Figure 5: Skin friction c_f versus streamwise location R_x for $Ma = 4.8$, free stream temperature $T_\infty = 55.4K$ and constant wall temperature $T_w = 270K$ with a shock angle of $\sigma = 14^o$.

The second case presented here is a boundary layer at $Ma = 4.5$ with a free-stream temperature of $T_\infty = 61.58K$ and insulated wall. For this case, the behaviour of the boundary layer with larger disturbances, which exceed the linear disturbances of the former case at $Ma = 4.8$ will be shown. The shock angle of the impinging shock wave here is $\sigma = 15^o$, which again produces a steady separation bubble.

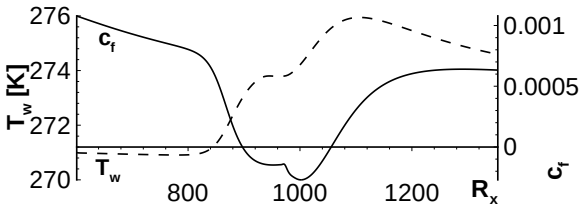

Figure 6: Skin friction c_f and wall temperature T_w versus streamwise location R_x for $Ma = 4.5$, free stream temperature $T_\infty = 61.58K$ and insulated wall. Shock angle $\sigma = 15^o$.

In Fig 6, the skin-friction coefficient c_f and the wall temperature distribution T_w is given for this second case. The skin-friction coefficient indicates that the separation bubble at the wall ranges from $R_x \approx 900$ to $R_x \approx 1060$. At separation and reattachment, the wall-temperatrue rises. However, the total temperature rise from the flow before the interaction region to the flow behind the interaction region is only in the order of $\approx 5K$. An increasing Ma-number and/or increasing shock strength would also increase the magnitude of the temper-

ature rise. The trend of the wall-temperature distribution is similar to the shape of the wall-pressure distribution, which has a plateau inside the separation bubble as well.

Influence of Small Disturbances Based on the linear stability theory for compressible flows, which was put into its present formulation by (Ref 16), results of the boundary layer with $Ma = 4.8$ and $\sigma = 14^o$ will be shown here. For this purpose, in the case with shock, local temperature and mean-velocity profiles and their respective first and second derivatives were extracted from the results of the direct numerical simulation of the base flow. Then, these local data-sets were fed into the linear stability equations. The results are shown in Fig 7 and in Fig 8, with the amplification rate $-\alpha_i = \partial\, ln\frac{A(x)}{A_0}/\partial x$, where $A(x)/A_0$ is the amplitude ratio of any flow variable.

In flows at higher Ma-numbers, several instability regions with respect to the disturbance frequency are present. The first two such regions are of great importance for the stability behaviour. The one at lower frequencies, the so-called first mode has smaller amplification rates than the second or first Mack mode at higher frequencies. In the case without shock in Fig 7 at $R_x = 1400$, the first mode ranges from $F \approx 0$ to a F slightly smaller than $F = 10^{-4}$. Towards higher frequencies a gap without amplification is followed by the second mode instability region, which expands up to $F \approx 1.6 * 10^{-4}$. As one can see here, the maximum amplification rates of the second mode are significantly larger than those of the first mode.

The shock wave, that hits the boundary layer at $R_x \approx 1360$ causes the amplification rates of the second mode to rise, while it shifts to lower frequencies within the interaction region. The clear distinction between the two instability regions as seen in the case without shock is lost. The first mode seems to vanish near shock impingement, while new instabilities are formed at frequencies above the present second mode close to the shock-impingement.

A comparison between linear theory results and direct numerical simulations in which small-amplitude disturbances are introduced at the dis-

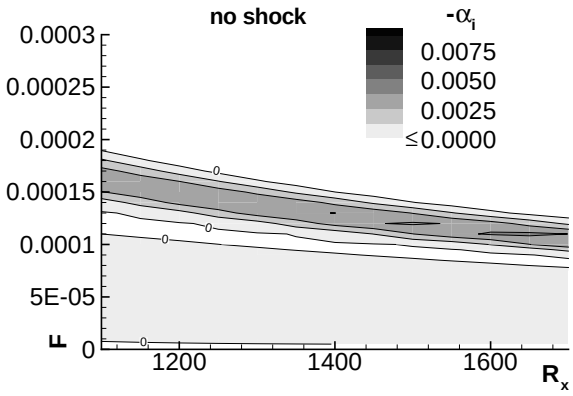

Figure 7: Linear stability for two-dimensional disturbances. Shown are results for the case without shock. R_x is the streamwise location, while F represents the disturbance frequency.

turbance strip are shown in Fig 9. The maximum disturbance amplitudes of the direct numerical simulation are obtained with a Fourier analysis in time over the last disturbance period of the simulation.

In Fig 9, results for two flow-variables (p and T) are shown. The maximum disturbance amplitude for the temperature typically describes the disturbance behaviour for disturbance amplitudes, which are located in a more distant position to the wall. On the other hand, the wall pressure amplitudes represent disturbance amplitudes at or near the wall. That way, the disturbance behaviour of the boundary layer can qualitatively be described with the two above quantities p and T, considering their particular distance to the wall. In general, disturbance amplitudes in a further distant location from the wall show better agreement with linear stability theory than wall-near amplitudes, because at or near the wall, non-parallel effects become larger. However, non-parallel effects, which are not considered in linear stability theory are present at more distant positions from the wall, too. They are responsible for the differences between linear theory and direct numerical simulation in both cases with and without shock in the maximum temperature disturbance amplitude-curves in Fig 9. To summarize, the results of the direct numerical simulation with small perturbations were validated by compressible linear stability the-

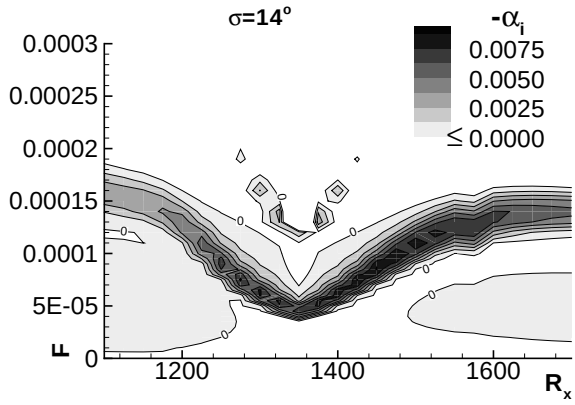

Figure 8: Linear stability for two-dimensional disturbances. Shown are results for the case with shock (shock angle $\sigma = 14^o$). R_x is the streamwise location, while F represents the disturbance frequency.

ory despite considerable non-paralle effects, which are already present in a boundary layer without shock and excluded from standard linear stability theory. This also applies for three-dimensional disturbances (not shown here) with smaller obliqueness angles, while for larger obliqueness angles, the agreement with linear theory increasingly deteriorates. This is also known for flows of that kind without shock-boundary layer interaction.

Influence of Larger Disturbances In this section, the behaviour of a boundary layer in the presence of larger amplitudes compared to the linear case in the section before is investigated. The conditions were chosen to generate only weakly nonlinear behaviour which can be classified as secondary instability. A good insight into the properties of this transitional stage, based on secondary instability theory calculations for the flow case presented in this section without impinging shock wave can be found in (Ref 8). In the following, (h, k) represents a mode of the frequency $h*F_0$, where F_0 is the fundamental disturbance frequency and a spanwise wave number $k * \beta$, with β as the fundamental spanwise wave number. The following figures in this section show the results of a time-wise Fourier analysis of the last simulated disturbance period. Three non-linear scenarios are considered. The fundamental case, where a two-dimensional primary disturbance wave $(1, 0)$ and a three-dimensional secondary disturbance $(1, 1)$ are introduced at the disturbance strip with the same disturbance frequency. In the subharmonic case, a primary disturbance wave $(1, 0)$ and secondary disturbance wave $(1/2, 1)$ with half of the frequency of the primary wave are introduced into the boundary layer, while in the oblique scenario, the boundary layer is perturbed with one three-dimensional wave $(1, 1)$. The modes $(1, -1)$ and $(1/2, -1)$ are perturbed as well in the fundamental, subharmonic and the oblique scenario, respectively, but not explicitly discussed. Due to symmetry assumptions, they are equal to their corresponding counterparts $(1, 1)$ and $(1/2, 1)$.

The upper picture in Fig 10 shows results for the temperature fluctuations of the subharmonic simulation. Here, $F_0 = 1 * 10^{-4}$ and the obliqueness angle $\beta = 25$. For comparison, the dotted lines with symbols refer to simulations without impinging shock-wave. Behind the interaction region the disturbance amplitudes of all modes are larger than the corresponding values in the case without shock. The amplitudes of the $(0, 2)$ mode, which in terms of the spanwise wave number $k*\beta$ is the first streak- or vortex mode created in the subharmonic scenario, becomes significantly larger than in the case without shock. Its increase also exceeds the rise of the primary and secondary disturbance amplitudes of the same case. The lower picture in Fig 10 shows the phase velocities of the primary and secondary waves of the temperature disturbance with and without shock wave. The phase velocities indicate, whether the primary and secondary disturbances synchronize, which is a requirement for resonance. As can be seen, the two waves synchronise in both cases with and without shock, therefore the resonance condition is fulfilled. The synchronisation in the case with shock occurs downstream the separation bubble. Because of the effects induced by the shock, downstream $R_x \approx 820$ the disturbance waves are decelerated, then sharply accelerated at $R_x \approx 970$ and again decelerated from $R_x \approx 1000$ to $R_x \approx 1180$, from where they run downstream synchronously.

The fundamental case is represented in Fig 11. Again, $F_0 = 1 * 10^{-4}$ and the spanwise wave number of the secondary wave is $\beta = 25$. As in the

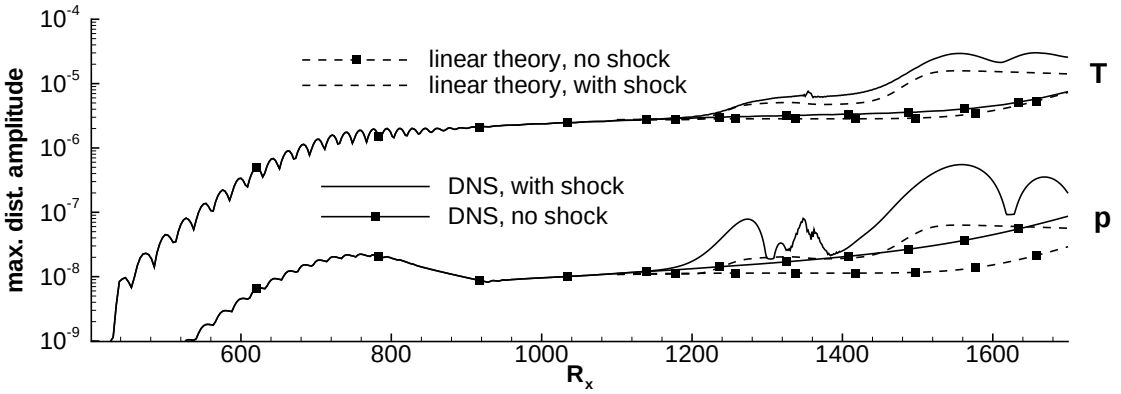

Figure 9: Comparison between linear stability theory results and direct numerical simulations results of the wall-pressure amplitude and the maximum temperature disturbance. $Ma = 4,8$ and $\sigma = 14^o$.

subharmonic case, the first vortex mode, which is $(0,1)$ here starts to sharply rise at $R_x \approx 1000$.

Figure 12 shows the temperature disturbance amplitudes for the so-called oblique scenario. This scenario is characterised by the interaction of two waves $(1,1)$ and $(1,-1)$. The fundamental disturbance frequency and spanwise wave number are the same like in the fundamental and subharmonic cases. As before, the vortex mode $(0,2)$ increases intensely from $R_x = 1000$ downstreamward and soon exceed the amplitude of $(1,1)$. Like the $(0,2)$, the other higher modes, which are generated by the oblique scenario, such as $(1,3)$ and $(0,4)$, increase in a similar manner. However, their initial magnitude is smaller than $(1,1)$ or $(0,2)$, therefore the amplitude at the outflow does not reach the magnitude of either $(1,1)$ or $(0,2)$. The similar growth of the vortex modes in all perturbation scenarios investigated suggests that the growth of the $(0,k)$-modes downstream shock-impingement is independent from the applied scenario.

The left picture in Fig 13 depicts vorticity ω_x and streamlines of the single $(0,2)$-mode at $R_x = 1100$. It indicates, that this modes correspond to a vortex.

However, the sum of the vortex mode amplitudes is still not large enough to produce a vortex in the total flow, as can be seen from the streamlines in Fig 14, which are not influenced. The results of Fig 14 were obtained by adding the modes $(0,0)$,$(0,2)$ and $(0,4)$ directly generated by the oblique disturbance scenario to the undisturbed base flow. Possible higher modes, such as $(0,6)$, $(0,8)$, etc. could be neglected, because their magnitude is very small.

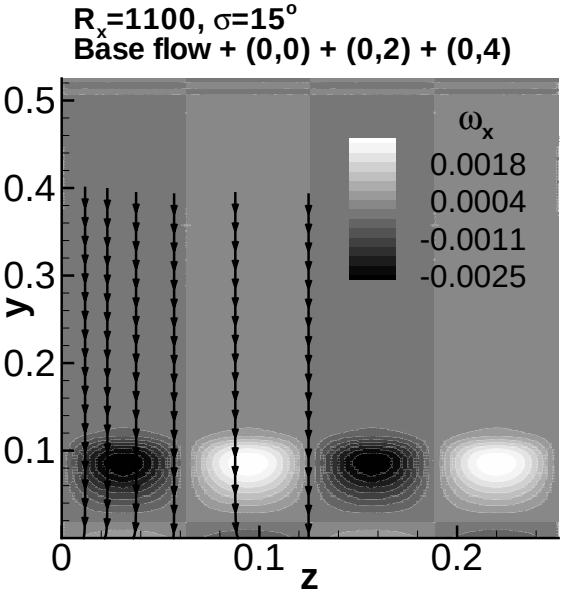

Figure 14: vorticity component ω_x of the modes $(0,0)$, $(0,2)$, $(0,4)$ added to the base flow at $R_x = 1100$ with selected streamlines for the oblique scenario.

The maximum of the wall-normal velocity of the base flow at $R_x = 1100$ is around 10^{-2}, while the magnitude of the disturbance flow is $\approx 10^{-5}$, as

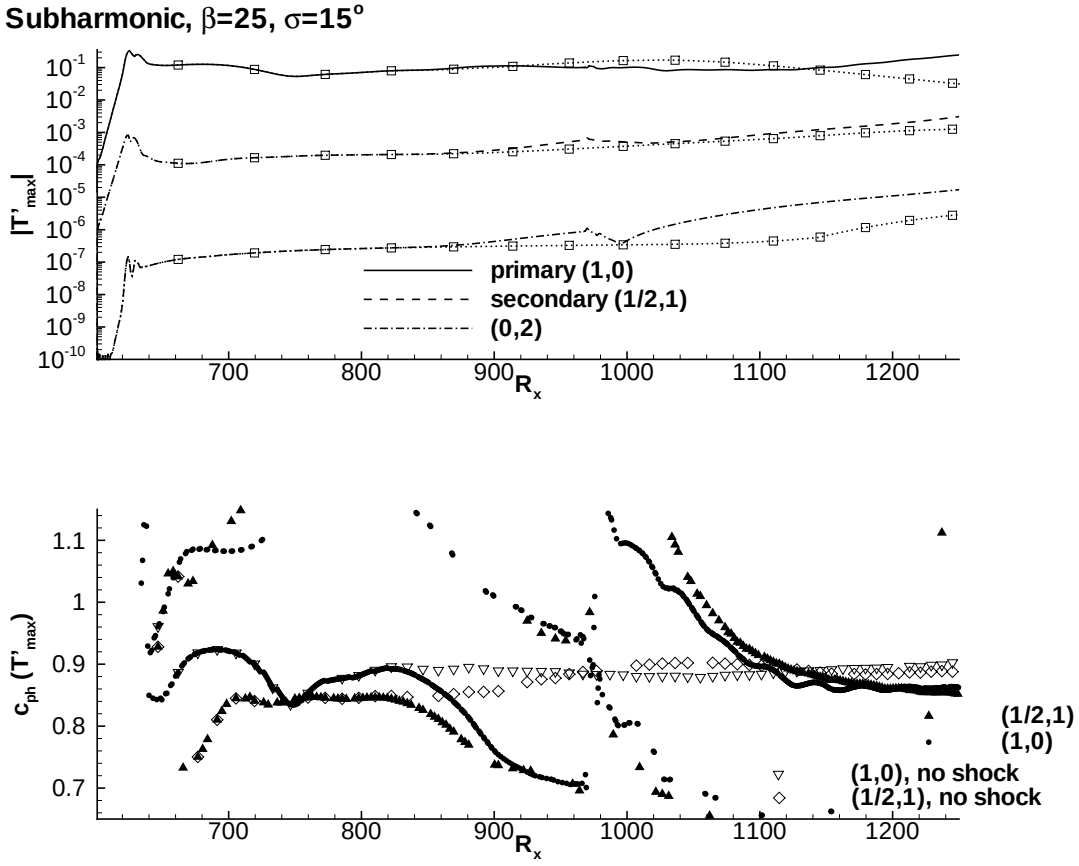

Figure 10: Modal representation of maximum temperature disturbance amplitudes for the subharmonic case.

can be seen in the right picture in Fig 13, which gives the disturbance velocity amplitudes for the first, therefore largest vortex mode $(0, 2)$.

In the case without shock, represented by Fig 15, vortices are also present in the $(0, 2)$ mode. However, the amplification of the $(0, k)$-modes in the case without shock is much smaller compared to the case with shock downstream shock-impingement. Also, the velocity profiles for the case without shock, which are given by the right picture in Fig 15 have a different shape than the velocity profiles for the case with shock in the right picture of Fig 13, especially the wall-normal velocity v. The position of the vortices with respect to the wall-normal distance y differs as well. While in the case with shock, the vortex-cores are located between the first and second maximum of the streamwise disturbance velocity w, the vortex cores in the case without shock are in a farther position from the wall, after the second maximum of w. This and the smaller amplification rates might indicate, that in the case with shock, a different vortex-development mechanism is present than in the case without shock.

As an explanation for the occurrence of such vortices in shock-boundary layer interactions, a Görtler instability is typically mentioned in the literature, e.g. (Ref 2, 3, 11). However, this is difficult to prove in a quantitative manner. In Fig 4, we clearly observe the concave curvature of the boundary layer near reattachment, which might trigger a Görtler instability (note that the figure is stretched in y-direction, thus not giving the physical scale).

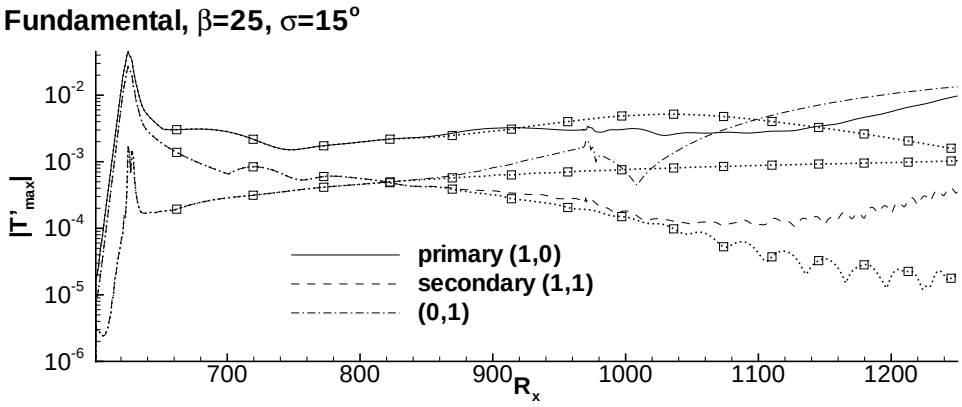

Figure 11: Modal representation of maximum temperature disturbance amplitudes for the fundamental case.

Conclusions and Future Research It was found, that for small disturbance amplitudes maximum amplification rates were increased and shifted to lower frequencies. The linear stability theory results agreed well with the corresponding direct numerical simulations. In the weakly non-linear case, a strong increase of the so-called streak- or vortex modes $(0, k)$ could be observed at and downstream reattachment independently of the disturbance scenario applied. A possible explanation for suchlike behaviour could be found in a Görtler-type instability mechanism, due to the concave curvature of the boundary layer in that flow-region. This, however, remains to be proved in a quantitative manner.

For the future, further research will be carried out in the non-linear regime with higher Ma-numbers and stronger shocks. Stronger shocks eventually yield unsteady separation bubbles, such as shown in Fig 16 for a two-dimensional simulation at $Ma = 6$. It is also intended to investigate possible control of the flow by means of specific large-amplitude disturbances.

Acknowledgement The authors would like to thank the *Deutsche Forschungsgemeinschaft* for supporting this research within *Sonderforschungsbereich 259*.

References

[1] J. Ackeret, F. Feldmann, and N. Rott. *Untersuchungen an Verdichtungsstößen in schnell bewegten Gasen*. Report no. 10, ETH Zürich, Institut für Aerodynamik, 1946.

[2] D. Aymer de la Chevalerie, L. De Luca, and G. Cardone. Görtler-type vortices in hypersonic flows: The ramp problem. *Experimental Thermal and Fluid Science*, 15:69–81, 1997.

[3] L. De Luca and G. Cardone. Viscous interaction phenomena in hypersonic wedge flow. *AIAA Journal*, 33:2293–2298, 1995.

[4] J. Délery and J.G. Marvin. Shock-wave boundary layer interactions. *AGARDograph*, 280, 1986.

[5] J.M. Délery. Shock phenomena in high speed aerodynamics: Still a source of major concern. *The Aeronautical Journal*, pages 19–34, January 1999.

[6] D.S. Dolling. Fifty years of shock-wave/boundary-layer interaction research: What next? *AIAA J.*, Vol. 39, No. 8:1517–1531, 2001.

[7] W. Eißler. *Numerische Untersuchungen zum laminar-turbulenten Strömungsumschlag in Überschallgrenzschichten*. Dissertation, Universität Stuttgart, 1995.

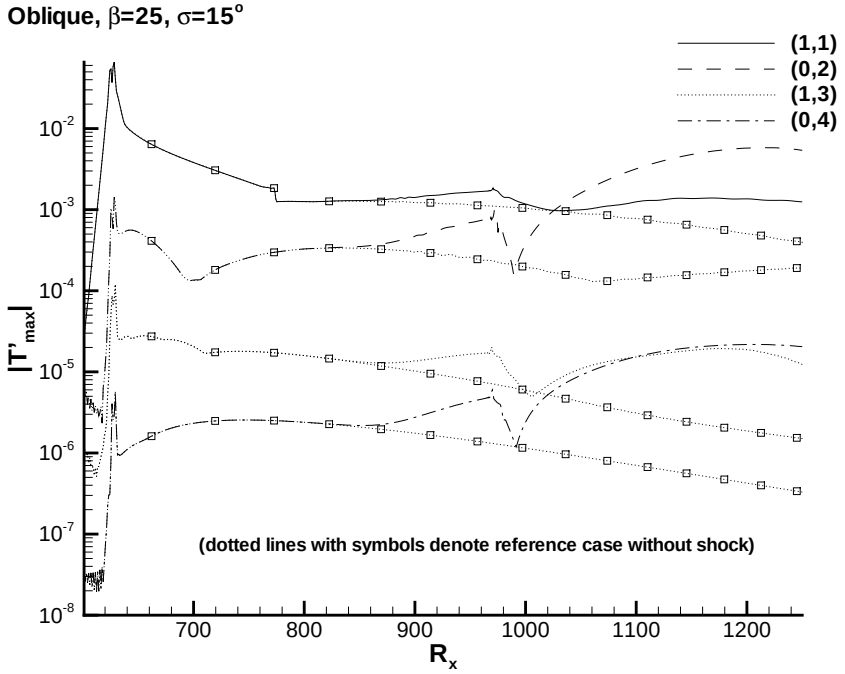

Figure 12: Modal representation of maximum temperature disturbance amplitudes for the oblique case.

[8] N.M. El-Hady. Secondary instability of high-speed flows and the influence of wall cooling and suction. *Phys. Fluids*, A 4 (4):727–743, April 1992.

[9] C.G. Graham and F.H. Kost. Shock boundary interaction on high turning transsonic turbine cascades. *Gas Turbine Conference and Exhibit, San Diego*, March 1979.

[10] P. Harris. *Numerical investigation of transitional compressible plane wakes*. Dissertation, University of Arizona, 1993.

[11] H. Henckels, A.F. Kreins, and F. Maurer. Experimental investigations of hypersonic shock-boundary layer interaction. *Z. Flugwiss. Weltraumforsch.*, 17, Heft 2:116–124, 1993.

[12] Th. Herbert. Secondary instability of boundary layers. *Ann. Rev. Fluid Mech.*, 20:487–526, 1988.

[13] L. Lees and C.C. Lin. Investigation of the compressible laminar boundary layer. *NACA Tech. Note*, 1115, 1946.

[14] S.K. Lele. Compact finite difference schemes with spectral-like resolution. *J. Comp. Phys.*, 103:16–42, 1992.

[15] H.W. Liepmann. The interaction between boundary layer and shock waves in transsonic flow. *J. Aeronaut. Sci.*, 13:623–637, 1946.

[16] L.M. Mack. Boundary layer stability theory. *Jet Propulsion Laboratory, Pasadena, Tech. Rep.*, 900-277, 1969.

[17] W. Saric, E. Reshotko, and D. Arnal. Hypersonic laminar-turbulent transition. *AGARD*, AR-319, 1998.

[18] K.W. Thompson. Time dependent boundary conditions for hyperbolic systems. *J. Comput. Phys.*, 68:1–24, 1987.

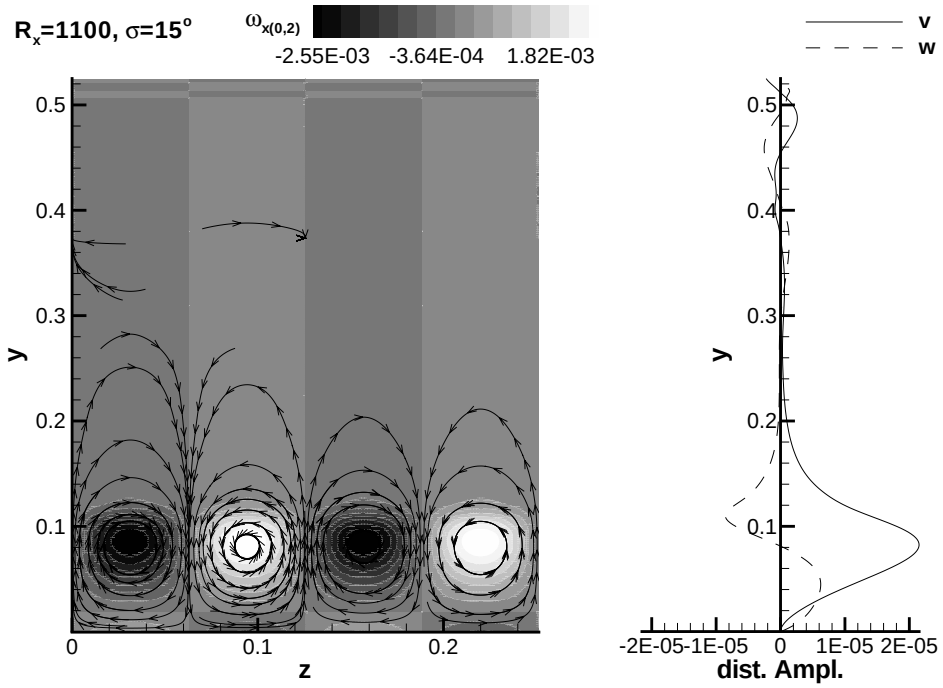

Figure 13: vorticity component ω_x of mode $(0,2)$ and disturbance velocity profiles at $R_x = 1100$ with selected streamlines for the oblique scenario.

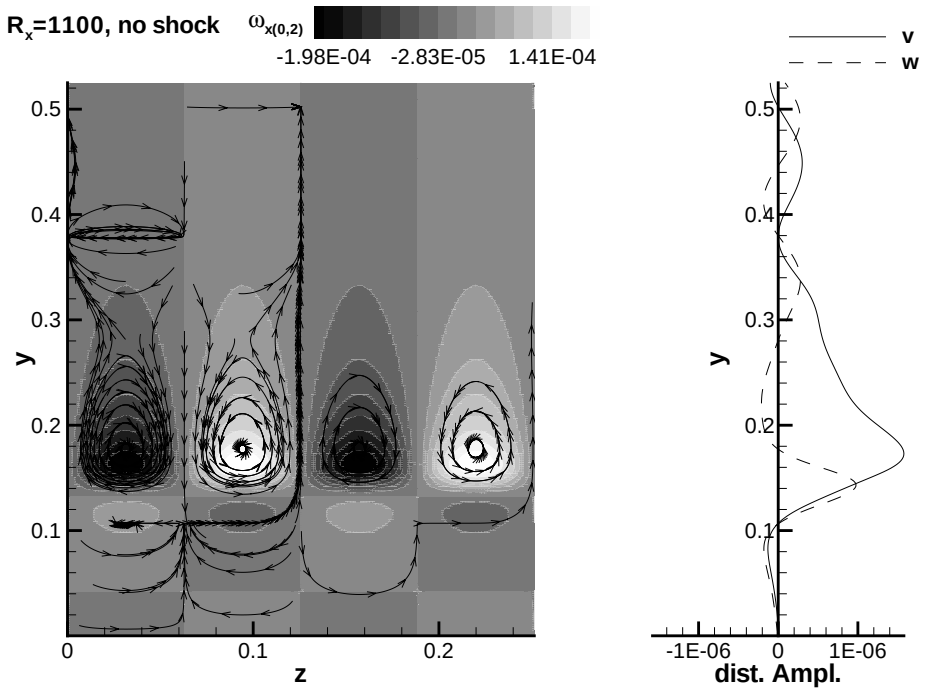

Figure 15: vorticity component ω_x of mode $(0,2)$ and velocity profiles at $R_x = 1100$ with selected streamlines for the oblique scenario.

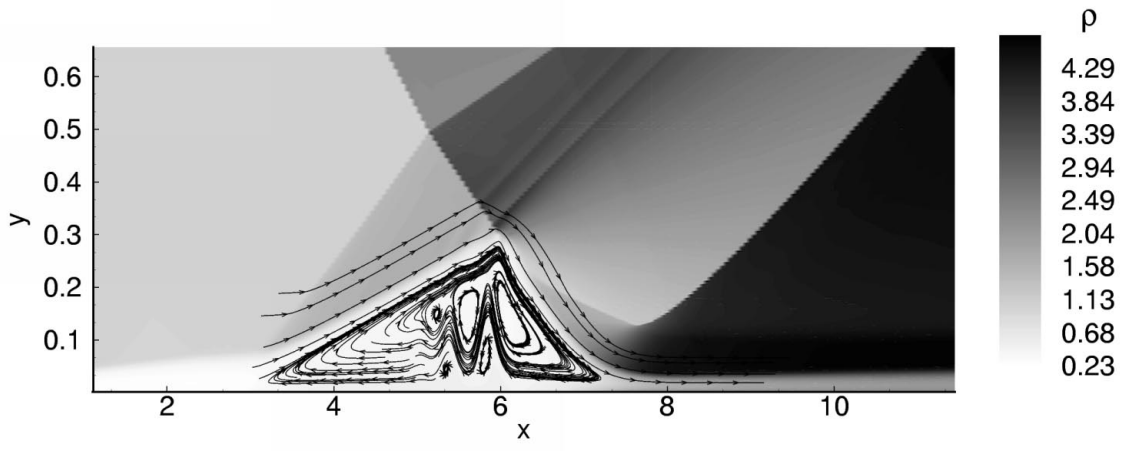

Figure 16: Density field and selected streamlines at $Ma = 6$ with $\sigma = 16.9^o$, $T_\infty = 55.4K$ and $T_w = 300K = const.$